WELDING RESEARCH

SUPPLEMENT TO THE *WELDING JOURNAL*, MARCH 1990

**Sponsored by the American Welding Society and the Welding Research Council**



# Computerized Radiographic Sensing and Control of an Arc Welding Process

*Real-time radiography is demonstrated to be a means of studying the arc welding and a method for adaptive control*

**BY S. I. ROKHLIN AND A. C. GUU**

ABSTRACT. The paper summarizes an effort in which real-time radiography was implemented for on-line arc welding process study and control. X-ray penetrating radiation was used for volume observation in the welding pool and the heat-affected zone during the weld process. The advantages of such a technique are on-line detection and monitoring of defect formation in the weld and capability to study metal fusion and filler metal/base metal interaction and metal transfer in the welding pool. This technique may also be used for postservice, real-time remote testing of weld quality.

A new concept of arc welding process control was developed based on using information on weld quality, received from automatic recognition of real-time radiographic images, in feedback for closed-loop weld control. This distinguishes the radiographic approach from more conventional methods where indirect information on weld quality is used.

The experimental system developed during this project integrates the welding apparatus and the real-time radiographic system together with a digital image processor unit and appropriate computers and software packages. Using this system, closed-loop process control was demonstrated through the control of weld penetration during submerged arc welding. Special attention was given to the evaluation of system parameters such as detectability and resolution.

Monitoring the welding process with real-time radiography may also provide new opportunities for studying arc welding physics. As an example, the metal transfer mode and plasma pressure cycle for submerged arc welding have been determined. Another potential application of the system may be for weld pool analysis, where on-line monitoring of the pool dimensions can be used for control of weld penetration.

**KEY WORDS**

Arc Welding Control
Computerized Control
Radiographic Control
Real-Time Radiography
Weld Quality Evaluation
Joint Penetration
Penetration Control
Submerged Arc Welding
Process Monitoring
In-Process NDE

## Introduction

Two different approaches may be applied to nondestructive evaluation of welds. The conventional approach consists of the application of nondestructive inspection after welding. The second approach, and one that provides more valuable information on weld quality, is in-process nondestructive evaluation where the production and testing operations are integrated into a single procedure. In this combined approach, information gathered during welding may be used in a feedback loop, together with other process parameters, for process control. Such a concept may provide significant cost savings (Ref. 1). An additional advantage of this approach is that the nondestructive system may be included as a part of the sensing system in the feedback loop of the process control system. This means that quality control may be integrated with the process itself.

Traditionally, the radiographic method of nondestructive evaluation of welds,

*S. I. ROKHLIN is an Associate Professor and A. C. GUU is a graduate student in the Department of Welding Engineering, Ohio State University, Columbus, Ohio.*

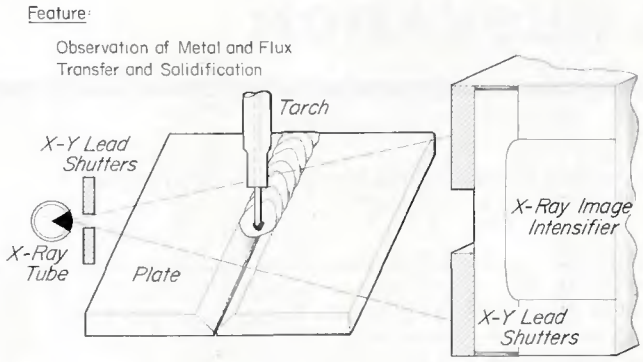


*Fig. 1—Schematic of horizontal setup for real-time observation of welding process.*

which uses x-ray penetrating radiation, has been widely used in industry for flaw detection. It has been used for both post-weld and in-service inspection. The main applications of radiography for characterization of weld quality may be categorized as follows:

1) *Conventional film radiography.* This technique has been widely used in the weld quality evaluation, primarily for post-manufacturing and in-service inspection (Ref. 2).

2) *High-speed radiography (or flash radiography).* This method is based on impulse x-ray tubes and high-speed x-ray films on which the image is formed during the period of duration of the x-ray pulse. Using this technique, a few very interesting studies have been conducted for understanding metal transfer in the weld pool. The use of flash radiography to study the mechanism of metal drop formation on the welding electrode was originally proposed by Becken (Ref. 3). Using an analogous method, Eichhorn (Refs. 4, 5) studied the submerged arc process. Using flash radiography, Bryant (Ref. 6) at Los Alamos National Laboratory, studied electron beam welding and reported data for weld penetration as a function of electron beam energy. Steinzel and Thomer (Ref. 7) provided examples of flash radiography applications for the arc welding process. These techniques have not received wide application because of difficulties related to very short times of observation and the long time required for film processing.

3) *Real-time radiography.* In recent years, a renaissance of radiography occurred, mainly due to developments in real-time radiography. Using this technique, the x-ray image may be observed on a TV monitor during exposure of the part to x-rays. The success of real-time radiography has become possible due to the development of high-quality image intensifiers and digital image processing. These have resulted in high-quality images comparable to high-quality film radiography. The main industrial application of real-time radiography is in the nondestructive evaluation of different structures after their manufacture (Ref. 2).

In this study, real-time radiography was implemented to provide in-process observation and control of arc welding. X-ray penetrating radiation was used for volume observation of the welding pool and the heat-affected zone during welding. The advantages of such a technique are on-line observation of defect formation in the weld and the study of metal fusion and filler metal/base metal interaction, metal transfer and mass flow in the welding pool. This technique may also be used for postservice real-time remote testing of weld quality. Finally, the application of real-time radiography to remote weld process control was demonstrated using a radiographic system as a vision system for manual and automatic recognition of the welding quality.

*Fig. 2—Schematic of vertical setup for real-time observation of welding process.*

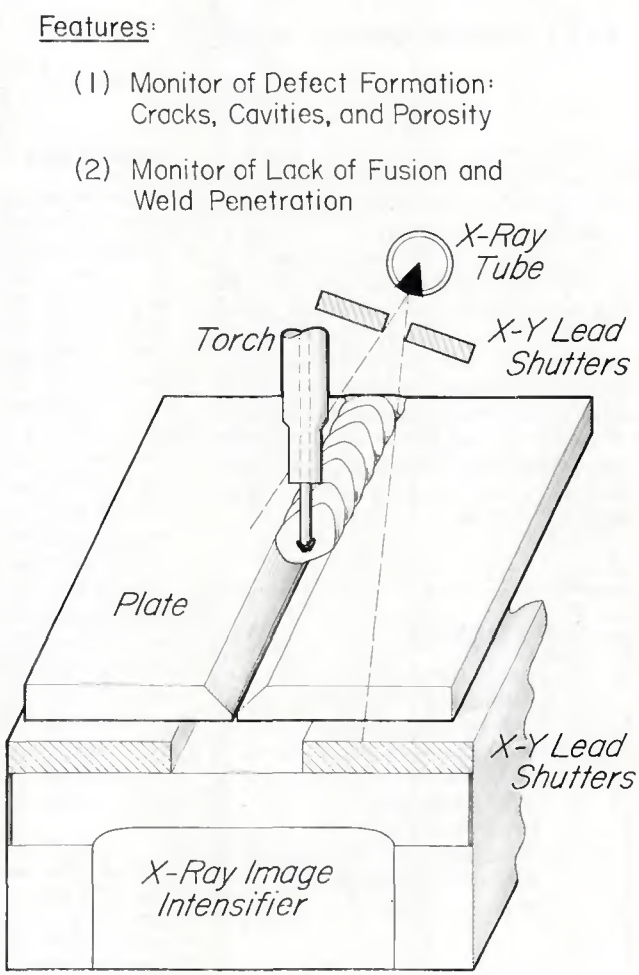


## Experimental Concept

Two system setups were used for real-time observation of the welding process: a horizontal setup shown in Fig. 1 and a vertical setup shown in Fig. 2. In the horizontal setup, x-rays parallel to the welded piece are received by the image intensifier from the side. This setup is appropriate for studying metal and flux transfer and solidification of the weld pool. Furthermore, testing in this position usually requires "soft" x-rays (about 30 to 50 kV) and, therefore, a miniature x-ray unit may be used.

In the vertical setup, the x-ray radiation is vertical or at small angles to the welding torch. This configuration is appropriate for studying discontinuity formation in the weld (cracks, cavities and porosities), and for monitoring incomplete fusion and joint penetration. It will also be shown that pool dynamics may be studied and monitored in the vertical configuration. The energy of the x-ray required in this case is usually higher than that for the horizontal orientation since complete penetration of the welding piece is required. For penetration

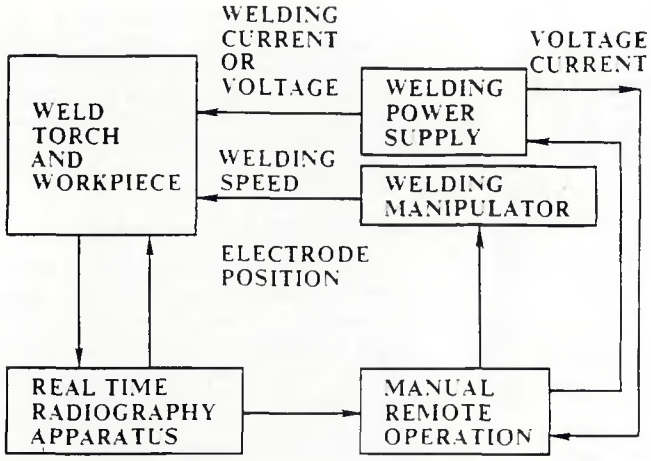


*Fig. 3 — Outline of concept for manual remote control of welding using real-time radiography.*

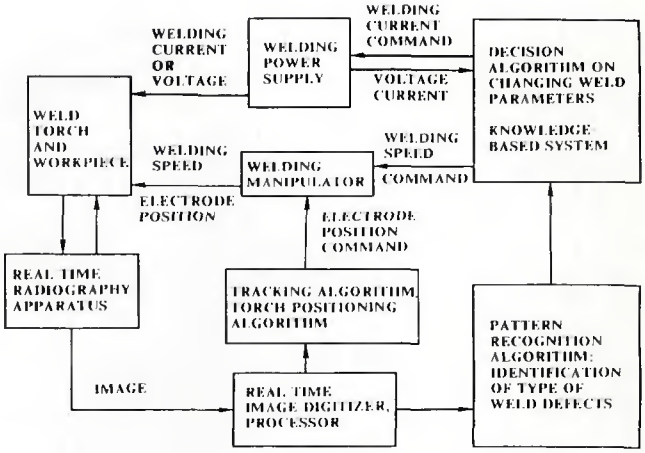


*Fig. 4 — Schematic diagram for intelligent automatic weld quality and process control with a radiographic system.*

control, a lower voltage may be used. As shown in Fig. 2, the x-ray unit was mounted above and the image intensifier below the welding piece.

The main advantage of the vertical method is that a real-time radiographic unit may be used as a vision system in feedback to the welding power supply, and it can be used simultaneously for on-line quality and process control. The outline of this concept for manual remote control is shown in Fig. 3. By using real-time radiography, welding is observed on a TV monitor and evaluated by the operator, who remotely controls the welding manipulator and the welding power supply, maintaining appropriate welding quality.

The radiographic method is distinguished from an optical vision system in two ways: 1) there is no effect of the welding arc on visibility and, more importantly, 2) internal discontinuities within the weld and the weld penetration are visible, thus providing information necessary for weld quality control. Automatic weld quality and process control are also possible in the framework of the radiographic method. A schematic diagram for such control is represented in Fig. 4. In this approach, the real-time radiographic image is digitized and analyzed by computer. The welding electrode position is clearly seen in the image together with the welding pool and the root opening (gap). As a result, one method of control may include tracking and welding gun positioning algorithms, which will control the welding manipulator.

Weld quality control is also possible, whereby the digitized image is analyzed by different pattern recognition algorithms for identification of weld quality and type of weld discontinuities (if they exist). Information on weld characteristics is then fed to the decision algorithm, which also interfaces with other sensors that analyze weld current, voltage and other parameters. The appropriate schedule for changing the welding parameters may then be established allowing, for example, appropriate current and weld speed variations to eliminate incomplete joint penetration. The knowledge-based system for different kinds of welding should be a major part of the decision algorithm.

In the work to date, only part of this general objective has been accomplished. Decision and pattern recognition algorithms were developed for a specific task, namely control of weld penetration. Incorporation of other types of discontinuities will require major development for automatic recognition of welding discontinuities.

## Experimental System and Procedure

### Experimental System

The schematic diagram of the experimental system is shown in Fig. 5. The real-time x-ray and welding units are integrated as a single setup in an exposure

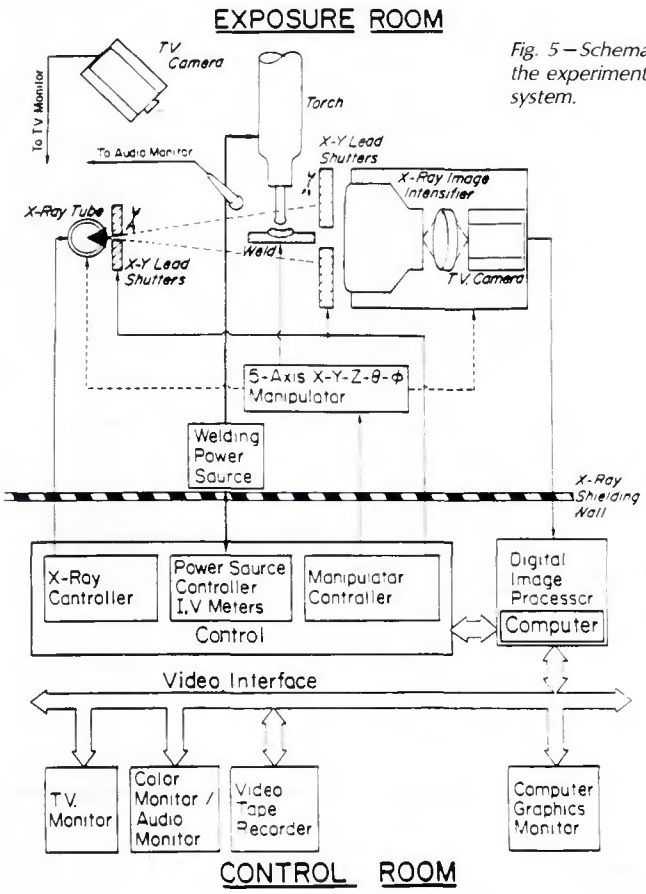


*Fig. 5 — Schematic of the experimental system.*

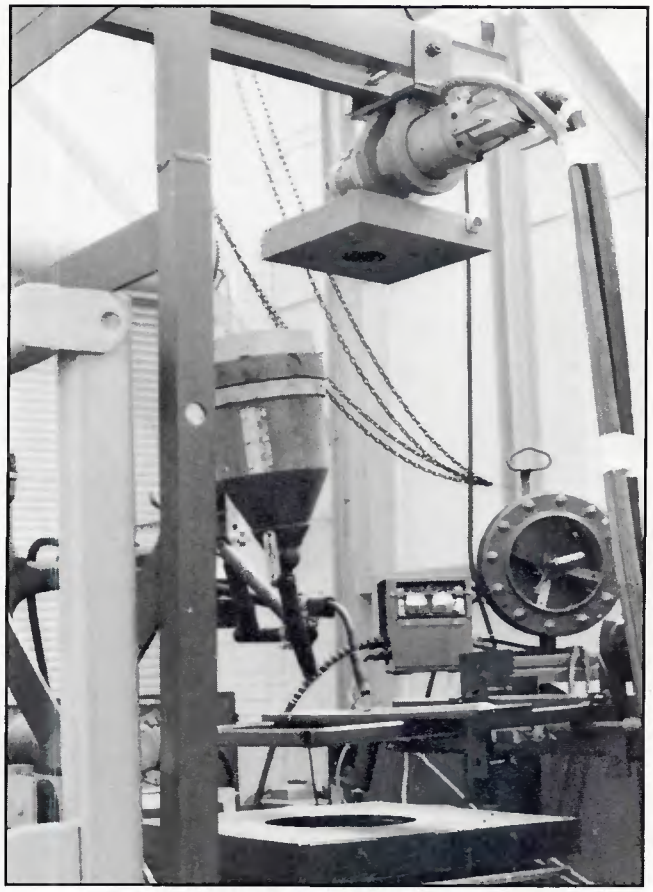

*Fig. 6 — Vertical setup showing the 160-kV x-ray unit (top), image intensifier (bottom) and welding apparatus.*

room. The radiographic system consists of exchangeable 160 and 300 kV x-ray sources and a Machlett lab image intensifier. The x-ray sources and the image intensifier have remote control x-y lead shutters to reduce the effect of scattered radiation on the image. The welding torch and workpiece are placed between the x-ray source and the image intensifier in a vertical or horizontal position depending on the mode of operation. The welding part is mounted on a 5-axis manipulator. The x-ray tube may be translated by the independent linear mechanical positioner. Both x-ray tube and image intensifier can be tilted and aligned relative to the welding part at the required angle of observation. The arc welding unit consists of a 600-A DC welding power source and a continuous wire feeding system. The welding power supply, manipulator and x-ray source are remotely controlled from the control room.

A TFI Gemini II control unit is used for the 160 kV ceramic tube and a Phillips control unit is used for the 300 kV tube. Radiographic image from the output of the image intensifier is picked up by a Vidicon television camera for observation and recording at the rate of 30 frames per second. Simultaneously, the television image is fed to a Quantex QX-9000 real-time image processor. It is used for image enhancement and for extraction of quantitative information on weld quality. A photograph of the experimental arrangement in the exposure room is shown in Fig. 6.

Real-time data on joint penetration, incomplete fusion and cavities are important for in-process adjustment of welding parameters, such as welding current and travel speed for improvement of welding quality. The digitized image may be analyzed in real time in the computer to make decisions about weld quality and subsequent welding power supply control. Examples of such closed-loop control of joint penetration are given in the following section.

**Table 1—Unsharpness (mm)**

| | FOV[a] Pixel | | Large Spot | | Small Spot | |
|---|---|---|---|---|---|---|
| M[b] | dy | dz | Ug[c] | U[d] | Ug | U |
| 1 | 0.21 | 0.22 | ~0[e] | 0.4 | ~0 | 0.4 |
| 1.5 | 0.14 | 0.15 | 1.4 | 0.5 | 0.2 | 0.3 |

(a) FOV = Field of view.
(b) M = Magnification.
(c) Ug = Calculated geometric unsharpness.
(d) U = Measured effective system unsharpness.
(e) ~0 indicates negligible unsharpness.

#### Evaluation of the Experimental System

Before performing radiographic measurements and radiographic inspection, the overall system performance was evaluated. Important system parameters such as detectability (minimal size of the flaw that can be found), resolution (minimal distance at which two flaws may be seen separately) and contrast sensitivity (minimal detectable thickness change of the sample) were selected as the basic system parameters. When these parameters are determined, it is possible to predict minimum flaw size in the weld that is detectable by a given radiographic system. The results of this study are general in nature and the methods developed may be applied to any radiographic system.

#### Unsharpness, Resolution and Spectrum Response

The system unsharpness is a combination effect of individual unsharpnesses of the radiographic channel such as geometric unsharpness, pixel size (only for digital images) and screen unsharpness. Certainly, larger individual unsharpnesses will yield a larger system unsharpness value.

A thin lead plate 50 microns thick with sharp edges was used to measure the effective system unsharpness. Figure 7 shows a typical edge spread function obtained from the real-time radiographic system. An effective unsharpness is calculated at the (1-1/e) level from the brightness contrast at the center of an edge spread function. The incorporation of this value gives good results in exponential fits of the real edge spread function. Table 1 presents the measured effective system unsharpness value and the calculated geometric unsharpness at different magnifications.

For the calculated geometric unsharpness, Ug, the (full) unsharpness value was taken; in contrast, the effective unsharpnesses were used for measured values. The pixel size in terms of field of view (FOV) was the area of view corresponding to a digitized pixel.

For magnification equal to one, the geometric unsharpness was negligible for both the large and small x-ray source spots. In this case, the system unsharpness was limited by the image-intensifier unsharpness and the FOV pixel size. For higher magnification, the effect of geometric unsharpness, Ug, became stronger and the corresponding size of the FOV pixel became smaller. At a magnification of 1.5, the Ug for the large focal spot was

the dominating factor and resulted in a larger value of system unsharpness. For the small spot at a magnification of 1.5, Ug is comparable to the pixel size, and the overall unsharpness of the system will thus be relatively small.

To have a smaller system unsharpness value, each individual unsharpness, including Ug, FOV pixel size and screen unsharpness must be minimized. Usually, a balance between the geometric unsharpness and the FOV pixel size can be made by adjusting the magnification. The optimal system unsharpness is achieved when all individual unsharpnesses are of the same order.

The spectrum response is the frequency-domain representation of the unsharpness. It is quite intuitive to think that a smaller unsharpness value (sharper image) will give better response and higher resolution. Using a lead pattern of slots with different spatial frequencies, spectrum responses of the real-time radiographic system were measured—Fig. 8. Figure 8 is normalized to the response of the slots with higher spatial frequency, 10 lines/mm in this case. The spectrum response is similar to that of a low pass filter, with cutoff at 2.4 lines/mm, which is the system resolution.

#### Signal-to-Noise Ratio and Threshold Contrast Sensitivity

The contrast sensitivity is the major parameter of the radiographic system. It is determined by the minimal thickness decrement ($\Delta h$) of the part to be radiographed, which directly influences the smallest visible changes in the brightness ($\Delta B$) of the screen. It can be calculated (Ref. 8) as:

$$\frac{\Delta h}{h} = \frac{(1 + I_s/I_d)}{\mu \gamma h} \frac{\Delta B}{B} \qquad (1)$$

where $\mu$ = absorption in the material; $I_s$ = intensity of scattered radiation; $I_d$ = intensity of direct radiation; h = thickness of the part; B = brightness level on the TV screen corresponding to the given thickness of the sample, h; $\gamma$ = system gamma that characterizes the sensitivity of the image intensifier and TV system.

The threshold level of the brightness change $\Delta B$ is determined by the noise level of the system. Radiographic noise is mainly composed of two parts, quantum noise and noise from the radiographic imaging system (called device noise). Each possesses both spatial and temporal components. The statistical characteristics of noise can be expressed by the mean value and the standard deviation of the brightness level. For a perfect radiographic channel, every pixel will have the same gray level, and hence, the standard deviation will be zero.

A small change in the sample thickness leads to a small change in screen brightness, $\Delta B$. This change of brightness may be considered a signal since it carries useful information (an existing defect changes the thickness of the sample). Such a defect may be simulated by a shim with calibration thickness, $\Delta h = t$. The mean value and the standard deviation are regarded as the signal level and the noise level, respectively. The signal level of a shim on a plate can be obtained as follows:

$$S/N = (\bar{p} - \bar{s})/\sigma \qquad (2)$$

where $\bar{p}$ = mean brightness of the background plate; $\bar{s}$ = mean brightness of the background plate with shim; $S = \bar{p} - \bar{s}$, brightness change due to shim (signal); $\sigma$ = standard deviation.

It is expected that maximum tube current would give the best S/N ratio and hence, the best minimum visible contrast sensitivity because the S/N ratio is proportional to the square root of the number of incident photons. The highest S/N ratio for a 2% shim on 6.35-mm-thick (0.25-in.) steel plate was obtained using 110 kV and 25 mA. The 2% shim was selected to find the opitmal current because it can be observed easily by the operator. Averaging of 20 frames was used to reduce the noise level.

Using the x-ray tube voltage and current selected, the signal and noise level for several shims were obtained. The data are presented in Table 2. For a small range of shim thickness change, the ratio of the brightness variation, $\Delta B$, to the shim thickness, t, is approximately constant (see last column in Table 2), where

$$t/\Delta B = \text{constant} = 0.012 \qquad (3)$$

If one takes the threshold level for visible

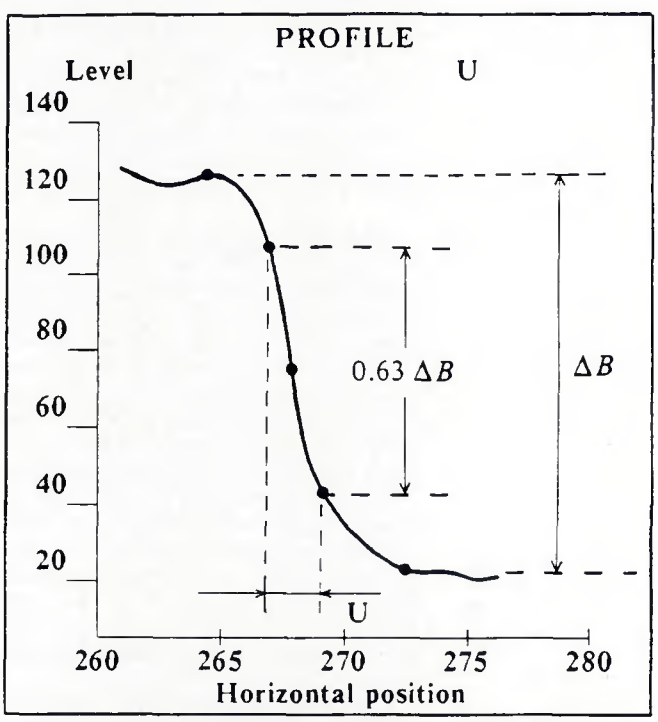


*Fig. 7—Typical edge spread function obtained from the experimental setup. Brightness level on vertical axis, distance (in pixels) perpendicular to edge on horizontal axis.*

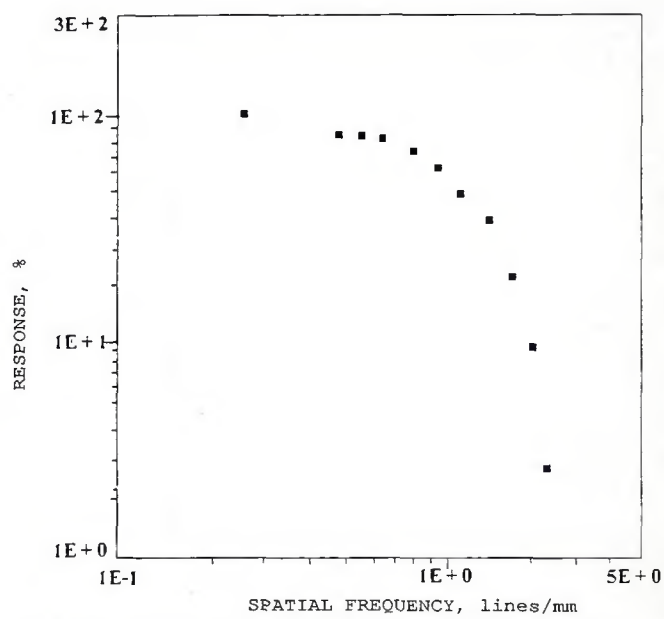


*Fig. 8—Experimental data for system frequency response. Cutoff frequency on right side characterizes extreme resolution of system in lines/mm.*

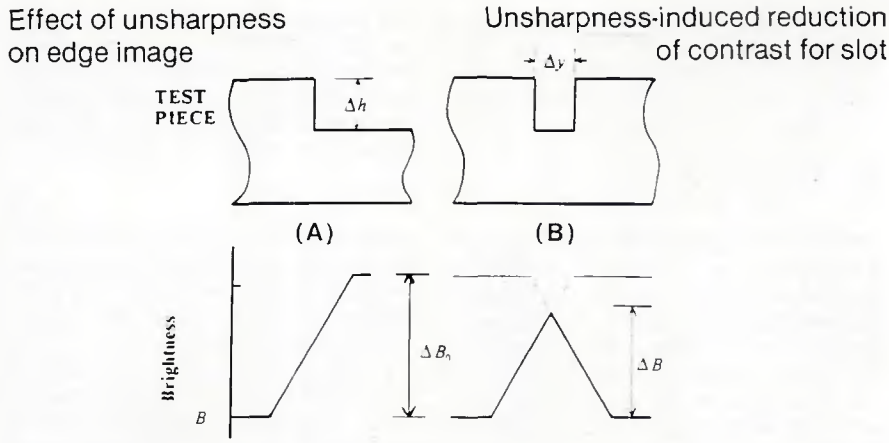


*Fig. 9—Effect of unsharpness on edge image and unsharpness-induced reduction of contrast for slot.*

brightness, ΔB, equal to 2σ, then the corresponding threshold shim thickness may be found as follows:

$$t^*/2\sigma = t/\Delta B = 0.012 \quad (4)$$

This gives the value 1% for contrast sensitivity, t*/h, where h is the thickness of the background plate.

The shim threshold thickness, t*, was also found directly by decreasing the shim thickness up to a value at which it became invisible on the screen to the human eye. The 1% value was confirmed by such direct measurements.

#### Detectability

Detectability may be defined as the size of the smallest visible defect. In particular, this size may be less than the pixel size. In this case, only the existence of the discontinuity may be determined from the image while its actual size cannot be found. Detectability depends not only on the size of the flaw in the plane of the image, but also on its thickness. Therefore, detectability and contrast are interrelated.

The contrast sensitivity, as discussed in the previous section, is a radiographic characteristic for a large-area flaw (for example a shim). For a small flaw, the effect of unsharpness will reduce the contrast sensitivity, as illustrated in Figure 9, where it is shown that the contrast of a narrow slot was decreased due to system unsharpness (so-called unsharpness-induced contrast reduction, Ref. 8.) In Fig. 9, the edge-spread function is drawn as a straight line for simplicity.

The dependence of the minimal visible size in an image plane of the flaw on the defect contrast is called the detectability curve (the defect contrast is defined below). The detectability curve of the long, narrow slot can be derived theoretically. As seen from Fig. 9, the brightness reduction due to unsharpness is:

$$\frac{\Delta B}{\Delta Bo} = \frac{\Delta y}{U} \quad (5)$$

where Δy is gap width and all other values are clear from Fig. 9. Therefore, the actual contrast of the flaw, C, will be less than expected value $C_o = \Delta h/h$ for a given flaw thickness Δh.

$$C = C_o\frac{\Delta y}{U} \quad (6)$$

To see a small flaw, the actual contrast, C, has to be equal to or greater than the threshold contrast sensitivity, C*:

$$C = \frac{\Delta h \Delta y}{hU} \geq \frac{\Delta h^*}{h} = \text{constant} \quad (7)$$

where Δy = width of gap; Δh/h = expected contrast; Δh*/h = threshold contrast (contrast sensitivity); U = system unsharpness.

It is necessary to distinguish clearly between contrast sensitivity, C*, (threshold contrast level corresponding to the minimal thickness of a large-area flaw, which is still visible on a screen) and contrast of the given flaw, C, determined by Equation 6. Using the equals sign, the threshold detectability curve can be drawn on a contrast-detail diagram taking the experimentally measured threshold contrast sensitivity, Δh*/h, as a parameter Δy against Δh/h.

Detectability was experimentally measured and compared with the estimated detectability curve—Fig. 10. The measurements were taken using calibrated shims—Fig. 11. For a given penetrameter thickness, Δh/h, the width of the gap between shims was reduced up to the point at which the gap became invisible on the image. The width of the narrowest visible gap is shown in Fig. 10 as a solid point. Invisible gaps are shown by open circles, apparent gaps by solid circles, and intermediate cases by half-solid circles. The detectability curve is the threshold contrast sensitivity for defects of different sizes. Above the detectability curve is the visible region; below it is the nonvisible region.

When the detail is larger than the system unsharpness, there is no contrast reduction. This is the point on the right end of the detectability curve. Physically,

**Table 2—Signal-to-Noise Ratio of Shims on 6.35 Steel Plate**

| Thickness | t/h % | σ Levels | ΔB Levels | t/ΔB |
|---|---|---|---|---|
| 0.025 mm | 0.4 | 2.3 | 2 | 0.013 |
| 0.076 mm | 1.2 | 2.3 | 7 | 0.01 |
| 0.127 mm | 2 | 2.5 | 10 | 0.013 |

*Fig. 10—Detectability curve for narrow slot. Theoretical curve is represented by the solid line.*

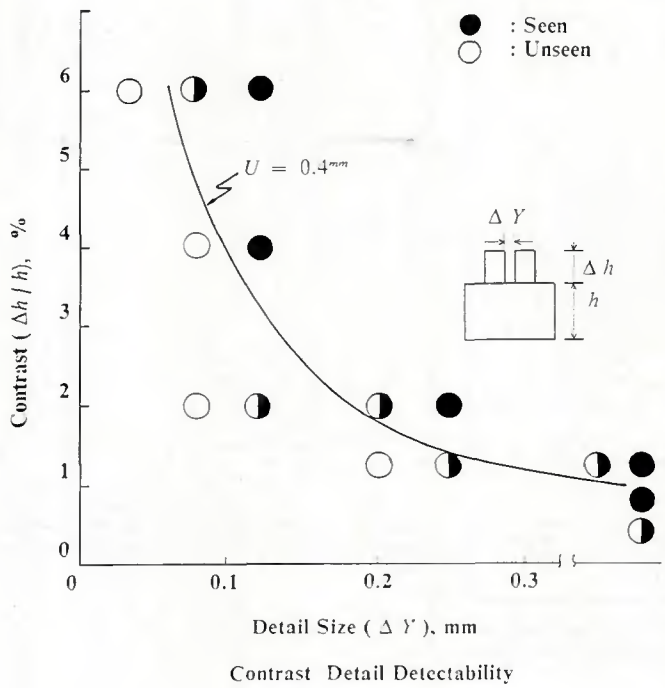

when the detail is smaller than the system unsharpness value, higher object contrast is needed for its observation on an image. This explains why the detectability curve for small detail rises to higher object contrast.

Using a detectability curve, evaluation of the quality of radiographic images is much more precise than using a penetrameter. The detectability curve gives the contrast sensitivity for different detail sizes and different thicknesses. The penetrameter represents only one point on this curve.

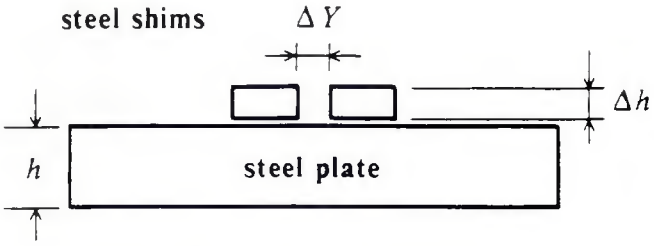


*Fig. 11 — Schematic of experimental sample for detectability measurements (calibrated steel shims and plate).*

#### Experimental Procedure for Manual Radiographic Monitoring of Submerged Arc Weld Penetration

The experiments were performed on groove welds made in the flat position by using the mechanized submerged arc welding (SAW) process. The weld was simultaneously monitored or controlled with the real-time radiography system. Prior to welding, the welding flux was placed at the top and bottom of the base metal — Fig. 12. All the samples were prepared from 356 × 50 × 6.35-mm (14 × 2 × 0.25-in.) mild steel. The welding wire was a continuous bare steel electrode 2.38 mm (3/32 in.) in diameter. A granular compound with a density of about 1.38 g/cm$^3$ was used as the welding flux. The density of the welding slag, which is melted and resolidified flux, was about 2.89 g/cm$^3$.

Complete joint penetration was required in this series of experiments. During welding, the welding current was varied between 340 and 390 A to obtain different depths of weld penetration. The arc voltage was held constant at 30 V and the welding travel speed was 6 mm/s (14.2 in./min). The depth of penetration was determined from the radiographic images. To determine the actual weld penetration, the welds were sectioned after welding. The width and thickness of the weld reinforcement and the depth of weld penetration were measured and compared with radiographic data. During the experiments, the radiographic exposure was initiated prior to welding to adjust the radiographic parameters (tube voltage and current) for optimal contrast. After the tube parameters were set, the welding was begun and radiographic images of the welding process were observed and recorded. The 160-kV x-ray tube was used for these experiments with 150-kV tube voltage and 5-mA tube current selected for process observation. The x-ray source and object were kept at a distance of about 180 cm (71 in.). Distance between the object and the image intensifier was about 19 cm (7.5 in.).

The real-time radiographic images were digitized and analyzed. Space averaging, histograms and image profiling techniques were used for image processing. An image profile is a distribution of the radiance value (value of gray level of the pixel) along a particular horizontal line of the image. For the image profiles of a weld in different cross-sections, the following weld geometries were calculated: the width and thickness of reinforcement of the weld, and the width and depth of inadequate weld penetration. The calculated weld geometries measured from the image profile were compared, as mentioned before, with the actual weld geometries measured from the weld cross-section.

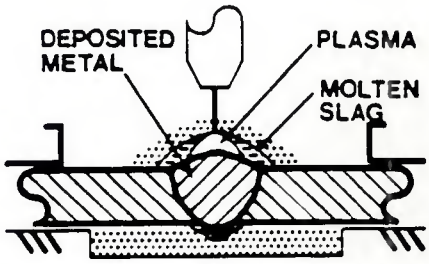


*Fig 12 — Schematic illustration of the submerged arc welding (SAW) process.*

#### Configuration of the System for Closed-Loop Process Control

One of the objectives of the study was to demonstrate the possibility of using real-time information from radiographic images for on-line feedback computer control of the welding power supply to maintain weld quality. The IBM AT computer with analog-to-digital (A/D) and digital-to-analog (D/A) boards was added to the system in Fig. 5 to control the welding power supply.

The schematic diagram of the measurement and control system is shown in Fig. 13. The image from the image intensifier is fed to the digital image processor, where the image is digitized and analyzed in real time. Specific features are extracted from the image and decisions on weld quality are made (for example complete or incomplete weld penetration). A packet of special programs was developed to operate the image processor for this purpose. Details of the algorithms are given in the next section.

The decision on weld quality is sent through an IEEE-488 interface equipped with A/D and D/A boards and used as a welding power supply controller. To control the welding power supply, the dial potentiometer used for manual remote control was replaced by a voltage-controlled potentiometer. This potentiometer was integrated on a special board controlled through a D/A converter by computer. The current and the voltage from the welding power supply were fed through a specially made signal conditioning and isolation board to the computer. The signals were digitized by using a 12-bit A/D converter. In addition, voltage and current were registered by the strip-chart recorder. In the computer, the current and voltage were smoothed to extract the DC component.

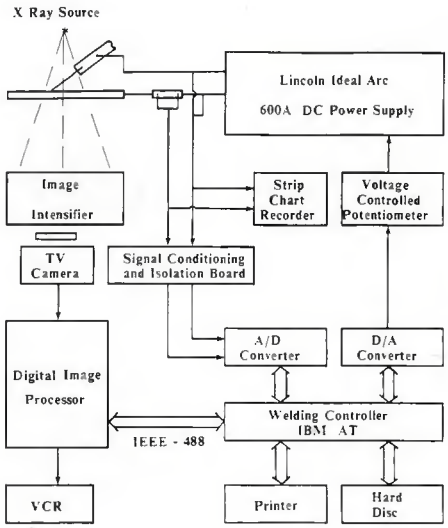


*Fig. 13 — Schematic diagram of the experimental arrangement for intelligent process control of welding. Several elements shown in Fig. 5 not included for simplicity.*

*Fig. 14 — A pseudocolor image for flux cored arc (FCA) welding.*

## Results and Discussion

### Metal Transfer and Pool Observation

Several experiments for observation of the metal transfer and pool dynamics were performed using the horizontal system configuration described in a previous section — Fig. 1.

As an example, a pseudocolor image for flux cored arc welding deposition is shown in Fig. 14. The cross-section of the weld deposition, which was done on a single plate, is seen as the dark-blue portion at the bottom of the figure. On the left side of the photograph are the torch and welding electrode. The drop on the electrode is the metal drop, which is ready to be transferred to the welding pool. There is also a drop from the electrode that bridges the electrode and the weld plate. Blue sparks of semicircular shape are flux transfers, and the flux (thin blue layer) covers the lower part of the electrode and the liquid pool (red). The red bulge on the right side is the metal buildup on the plate, which is still not completely solidified. The gaseous plasma is completely invisible in the image, but this is not so for submerged arc welding, as discussed below.

Most of the experiments were conducted using submerged arc welding. In this process, the welding pool is covered by a visually opaque powdered flux and, thus, other visualization techniques are of limited applicability. The submerged arc pool and the plasma bubble that surround the electrode are pulsating. A typical sequence of six images is shown in Fig. 15.

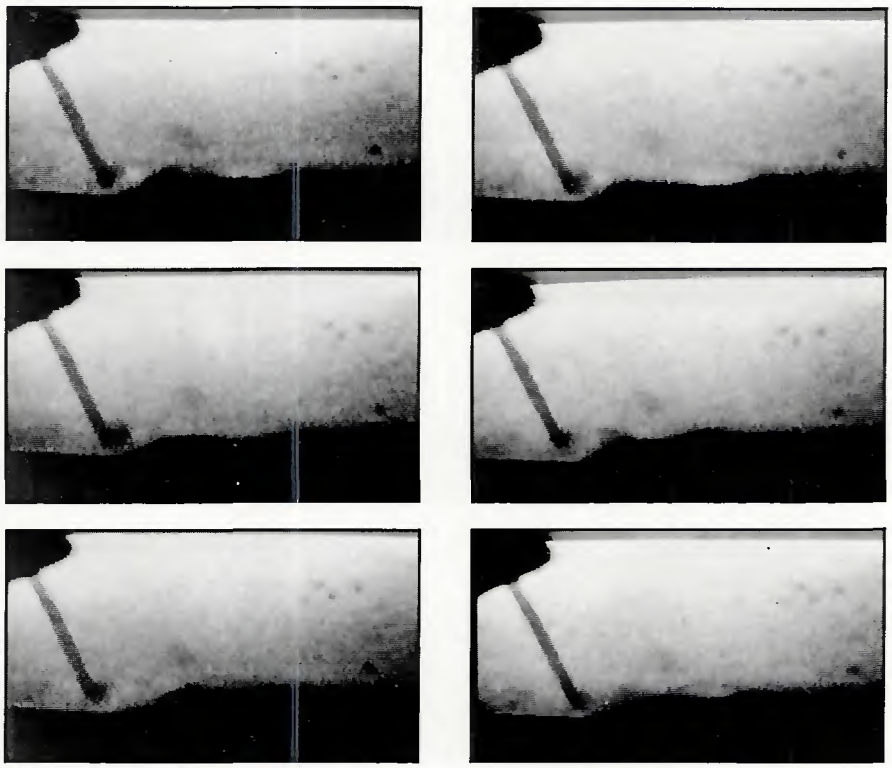

*Fig. 15 — Typical successive sequence of six images for submerged arc welding.*

On the left sides of the images, the end of the welding gun (upper-left corner) and the welding electrode (black) can be seen with the base metal in black at the bottom. The plasma bubble area may be observed for submerged arc welding since it has less absorption of x-rays than liquid flux and powdered flux, and it appears as a bright area close to the end of the electrode — Fig. 15A (in contrast to film radiography, it is shown as a positive image).

In the first image (Fig. 15A), the metal drop is beginning to form on the electrode. It is interesting to note that the melted region (on the right side of the electrode) has a soliton-type shape and the plasma area extends behind the soliton maximum. In Fig. 15B, the metal drop is more developed and the distance between the electrode and the melted area is becoming smaller. In the next image (Fig. 15C), the transfer of the drop from the electrode to the molten area has occurred. In the next stage (Fig. 15D), plasma pressure has built up in the electrode area leading to an increase of the distance between the electrode and the molten metal. This is clearer in the next image (Fig. 15E) where the shape of the edge of the molten area is becoming very shallow and the soliton-type shape has disappeared. At this stage, the cycle is complete and the next image (Fig. 15F) is similar to the first (Fig. 15A), which corresponds to the beginning of the formation of the metal drop. It is also evident that the plasma pressure had decreased since the distance between the electrode and the edge of the molten metal has decreased.

Experiments were also carried out in the vertical configuration (Fig. 2 and 6) for study of the pool dynamics. The corresponding results are described in a following section.

It is difficult to convey by a frozen image the actual visual impression that arises from the real-time radiographic weld image taken at 30 frames/s. This is the standard TV rate and is close to optimal for human visual perception. Integration of the high-speed TV camera with an image intensifier may be useful for this application, but it is not currently available in our laboratory.

### Manual Remote Control of Submerged Arc Weld Penetration by Radiographic Means

Change of welding conditions such as current, voltage, and/or speed of welding can affect the thickness and width of the weld reinforcement and penetration. In addition, these parameters influence the existence and degree of incomplete joint penetration. Incomplete penetration lowers the weld bearing capacity, and hence, is considered a weld defect. From the weld cross-section, dimensions of both the welding reinforcement and the inadequate joint penetration were actually mea-

sured. They were compared with the calculated values determined from the real-time radiographic images.

An example of a frozen image (one frame) from sequences of real-time radiographic images taken during submerged arc welding is shown in Fig. 16. The image is represented in positive form opposite to a film image. The base metal, the weldment and the melted pool are shown in the image. The weld and the pool are covered by the welding flux and by molten flux (slag). However, the flux affects an image only slightly because of its low density. The center dark region in the image is the weld. The upper part of this region corresponds to the weld with compete penetration. The lower part corresponds to the weld with inadequate penetration, which is seen as a long light strip along the joint. The lower dark area with the semicircular shape is the welding gun; the welding wire can also be seen. In front of the welding gun is the root opening, which is a totally white area. The surrounding gray area of weld is the base metal. The radiographic images were digitized in real time at the speed of 30 frames/s.

To establish a relationship between a gray level value of a pixel and the actual thickness of the material, the transfer function of the complete measuring system was determined by taking radiographic images of steel plates with slots of various depths and shims of various thicknesses. Steel plates of the same thickness as the base metal of the weldments were used. The slots simulate insufficient weld penetration, and the shims simulate weld reinforcements. The results of the measurements are summarized in Fig. 17, where the logarithm of the normalized value of the gray level is plotted versus slot depth or shim thickness, which are given in the deviations, $\Delta h$, from the original plate thickness, h. $B_2$ represents the value of the gray level in the images of the slot or shim, and $B_1$ is the gray level in the image of the plate. The data in Fig. 17 are well-fitted by a straight line that indicates a high dynamic range.

An example of data from a real-time radiographic image (as in Fig. 16) is shown in Fig. 18. The points corresponding to the weld reinforcement are in the upper part of the figure (increasing thickness) and the data for incomplete penetration are in the lower part of the figure (decreasing thickness). The straight line in Fig. 18 is the least square fit of the experimental data from

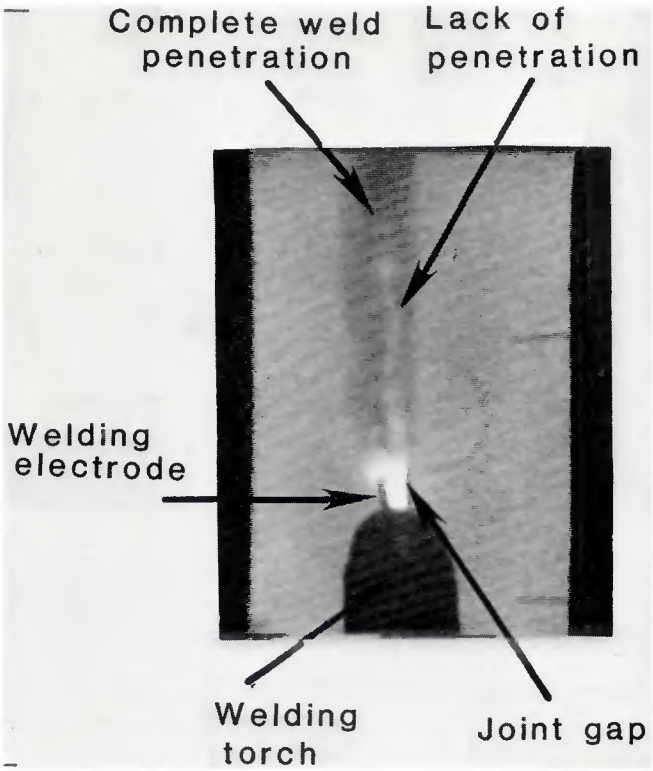


*Fig. 16 — Example showing one frame of the real-time radiographic image for submerged arc welding.*

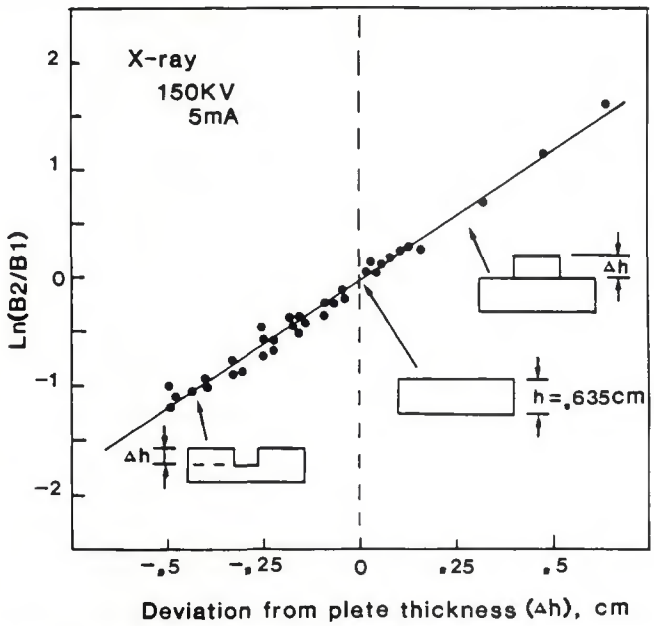


*Fig. 17 — Logarithm of the normalized gray level value versus slot depth and shim thickness ($\Delta h$).*

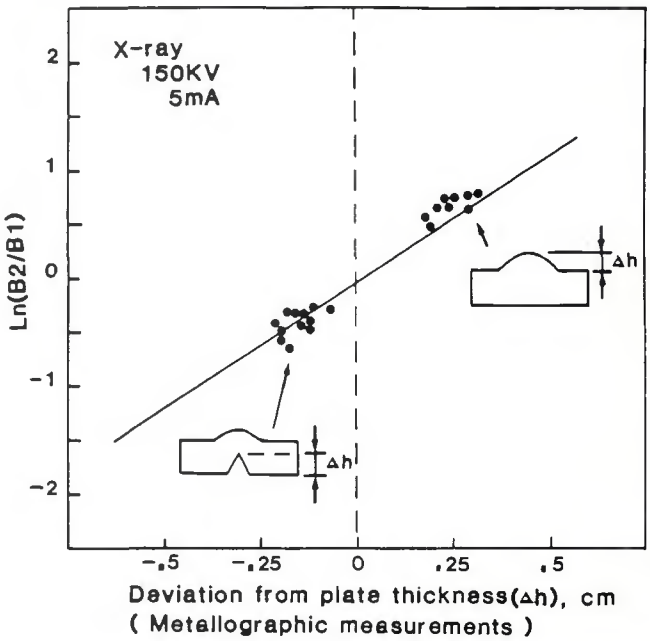


*Fig. 18 — Logarithm of the normalized gray level versus weld penetration and reinforcement ($\Delta h$) for actual weldments. The straight line is the least square fit of the experimental data from Fig. 17.*

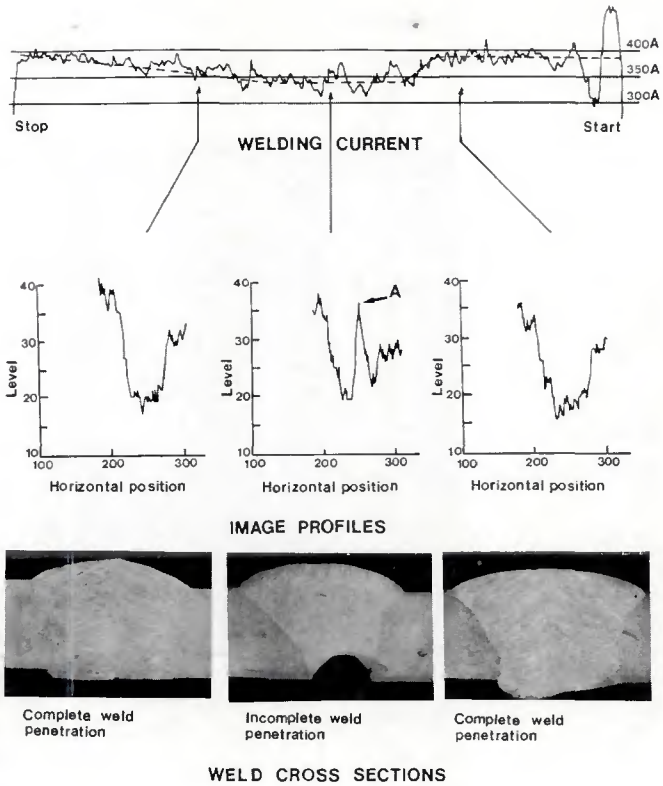


*Fig. 19 — Example illustrating process control. Using information received from image profiles, the welding current is readjusted in such a way that full penetration occurs.*

Fig. 17 (sample with slot and shims). The data from the actual weld are quite well fitted by this calibration curve. This example illustrates that the depth of joint penetration and thickness of weld reinforcement may easily be measured in real time.

Visual observation of real-time radiographic images and the digital information on depth of weld penetration received from these images were used for process control of the weld. For this, the welding current was adjusted in such a way that full penetration occurred. A typical example of the results of such an experiment is summarized in Fig. 19. Image profiles, in the middle portion of Fig. 19, show the changes of the values of the gray levels along a particular horizontal line of the digitized image. The deep, wide minimum of the profile corresponds to the increased thickness of the weld due to weld reinforcement. Units for the horizontal position in the image profiles are in pixels. One pixel is 0.2 mm for the selected field of view.

The lower part of the figure shows the photomicrographs of the weld cross-sections corresponding to the image profiles in the middle part. At a welding current of about 390 A, full weld penetration is observed. This follows from the image profile and is supported by the photograph of the weld cross-section, both shown in the right column. When the current is reduced to 340 A, there is incomplete joint penetration, indicated by the peak A on the center image profile. The depth of the joint penetration was calculated from the height of this peak, as discussed earlier. The information on incomplete joint penetration can be extracted from the appearance and height of peak A by computer. When incomplete penetration occurs, the welding current must be increased, as illustrated in the left column of Fig. 19. When the current is increased above 360 A, the peak A disappears, indicating full penetration, as is shown in the corresponding weld cross-section.

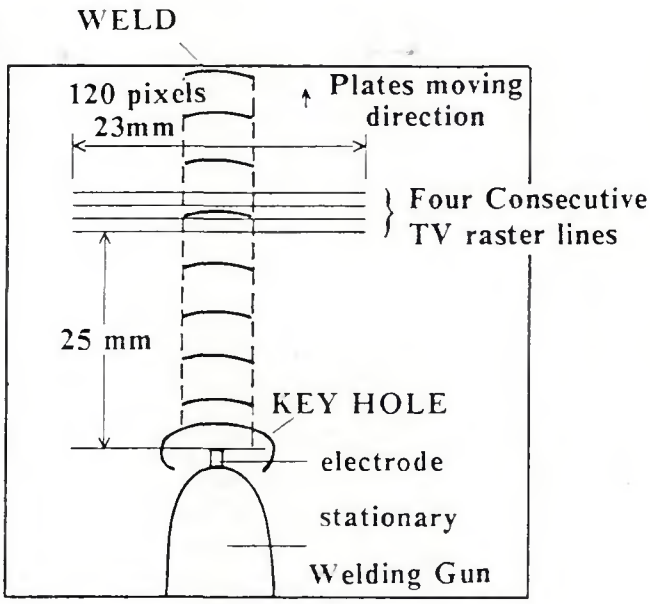


*Fig. 20 — Schematic diagram of the weld image showing the position of the window for image analysis.*

## Real-Time Computer Control of Weld Penetration

### Processing of Data and Outline of Algorithm for Computer Control of Weld Penetration

As was discussed previously, the information on incomplete weld penetration, which is visible as a bright line in Fig. 16, may be extracted from the shape of the pixel value (brightness profile, Fig. 19). In this section, an on-line computerized decision-making process for this feature is described. The difficulties of doing this lie in requirements for high-speed processing and noise reduction.

Brightness profiles were analyzed from the image at a distance of about 25 mm (1 in.) behind the welding gun to avoid the molten area, which is "noisy" due to pool oscillations. This distance is still small enough for a quick response on the weld quality and for corrections. One of the problems revealed in this early stage of the development was a high noise level in the profile traces. The noise complicates the finding of the profile maximum (Fig. 19), which should be done automatically by computer.

To reduce the noise level, significant space averaging and smoothing (low-pass filter) were done. First, four consecutive TV raster lines (Fig. 20) were digitized and averaged. The width of the digitized lines (window) was 120 pixels, which is equivalent to a line width about 23 mm (0.91 in.) across the weld. The sequence of averaging and smoothing is illustrated in Fig. 21, where the solid points correspond to one line of pixels (middle row in Fig. 21). Second, five neighboring pixels were averaged with the smooth profile shown by lowest line of 20 pixels in Fig. 21.

The profile represents smoothed brightness changes through the weld image. An example of such a profile in the part of the

weld lacking penetration is shown in Fig. 22A. The value $B_0$ corresponds to an increase of weld thickness relative to base metal area. The brightness $B_1$ characterizes the value of incomplete penetration. The value of the ratio $B_1/B_0$ is taken as one of the criteria for computer recognition of lack of weld penetration. It is compared to the threshold level, which is determined by the value of background noise. Full penetration occurs when $B_1/B_0$ is less than the threshold level. A typical image profile for complete weld penetration, after the above averaging procedure, is shown in Fig. 22B.

The second criterion selected for determination of joint penetration is based on the ratio of the area of the cross-sections $A_1$ and $A_0$ as shown schematically in Fig. 23. This value characterizes the cross-sectional area of the incomplete weld penetration. Based on these data, the thickness and width of weld reinforcement, and depth and width of incomplete joint penetration may be calculated from the radiographic image. Both the amplitude and the area criteria give information on depth and width of incomplete joint penetration.

The algorithms for decisions on the depth of penetration are schematically outlined in Fig. 24. The threshold levels were set either by radiographically examining previously made fully penetrated and incompletely penetrated welds or by calculation from the brightness-thickness ratio and pixel size. In this experiment, the threshold values were set to 0.1 for the brightness ratio, 18 mm$^2$ for the minimum reinforcement area and 0.1 for the area ratio. When any one of the above criteria was fulfilled, the joint penetration was judged incomplete.

#### Computer Control of Welding Experiment

The main distinguishing feature of the system is that information on weld quality extracted from the radiographic images is used in feedback for welding power supply control. Therefore, the first part of the system to be checked is the stability and effectiveness of the algorithm for measuring joint penetration. This was done by analyzing images recorded on a VCR during a typical experiment on monitoring joint penetration, described previously. The results of the decision on complete or incomplete penetration done by the computer program were superimposed on the recorded image and may be observed by the experimenter.

Thus, the validity of the computer decision may be compared with the visual perception of the operator. In such a way, the algorithm was debugged and the correctness of the threshold levels in its decision-making was checked. This is illustrated in Fig. 25, where the weld image is shown together with an overlay of the computer decision. In Fig. 25A, where the penetration is visibly incomplete, the computer decision is shown as "incomplete," as highlighted by a box. Figure 25B represents complete joint penetration. The decisions were based on a profile distribution taken along the white line shown across the weld.

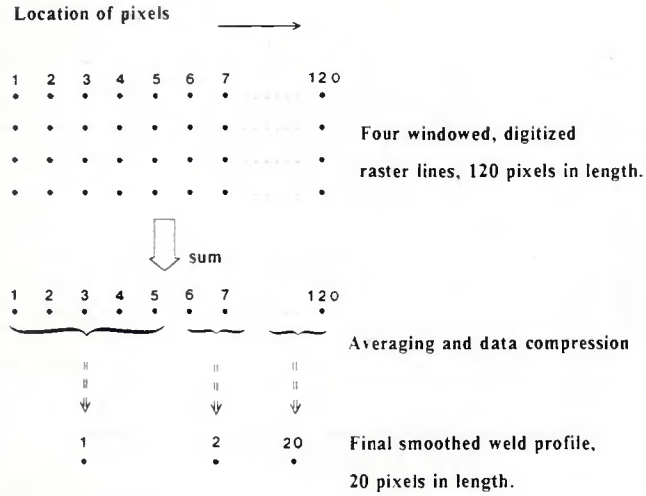


*Fig. 21 – Schematic diagram showing pixel arrangement in the window and the order of data smoothing and compression.*

The channels for measuring current and voltage were checked independently. Difficulties arose due to large random changes of current. In addition, signal filtering and smoothing were not a trivial problem. The effectiveness of the computer control of the power supply was studied separately.

To demonstrate the capability of the complete system, the following approach was taken. It was decided to force the system into the region of incomplete joint penetration and afterwards to lock it on automatic control and observe its recovery to the region of full penetration. For this purpose, in the initial stage of welding, the change of welding current was preprogrammed in the computer. Welding started in normal conditions. Then, the computer decreased the current and when an indication was received from image analysis of incomplete joint penetration, the feedback locked on and the computer began to increase the current in the power supply until the message "full penetration" was received.

Figure 26 illustrates the signal that controls the welding current, the actual measured welding current and a photograph of the weld sample with both top and bottom views. The welding current started at about 385 A (the command signal was 0.7 V), the welding voltage was about 30 V and the welding speed was 5 mm/s (12 in./min). Shortly after starting the welding arc, the welding current was rapidly decreased to about 350 A (command signal was about 0.55 V) to obtain simulated incomplete penetration. The feedback welding current command signal was increased by 0.05 V (roughly about 10 A in current) with each detection of incom-

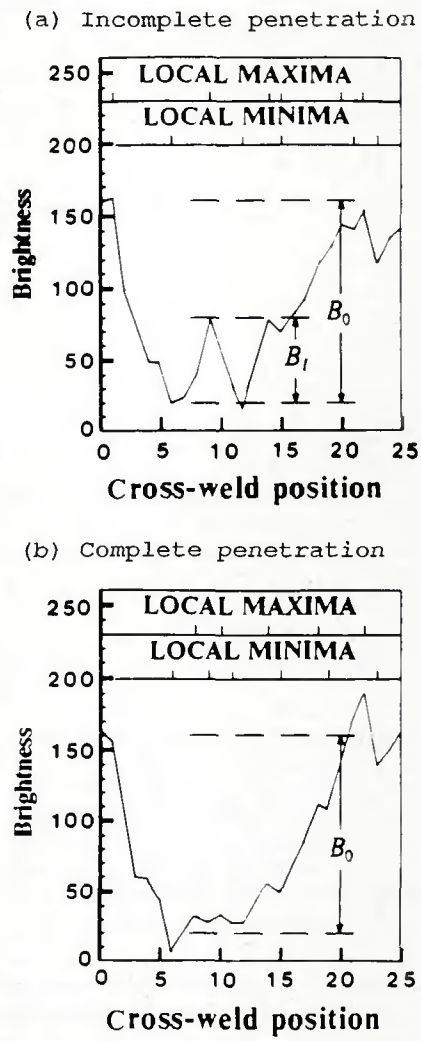


*Fig. 22 – Brightness profile across the image of the weld. $B_0$ is the difference in brightness levels between base metal and weld reinforcement. $B_1$ is the brightness difference between brightness levels of complete and incomplete penetration.*

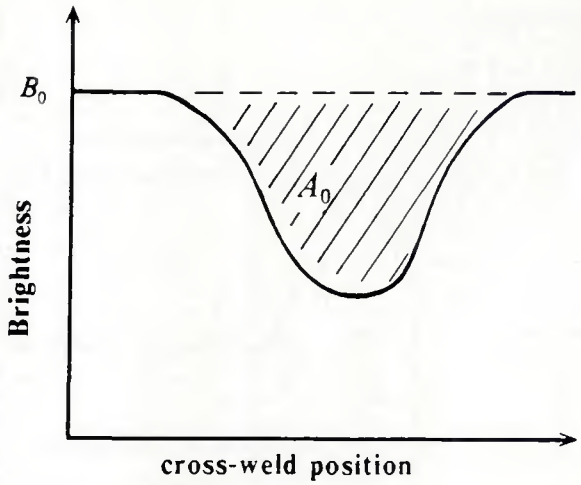


(a) full-penetration weld profile.

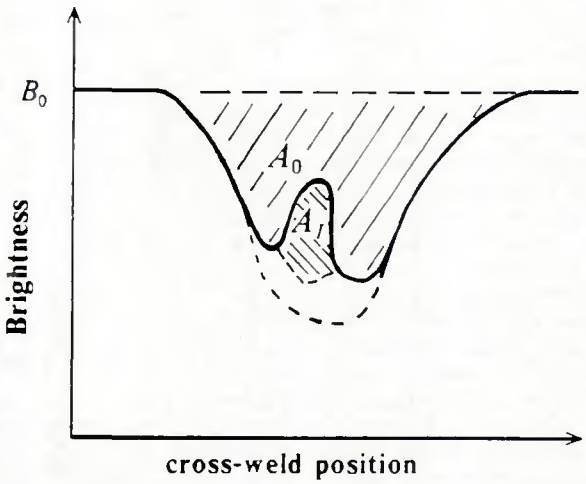


(b) Incomplete penetration weld profile.

*Fig. 23—Schematic showing the cross-sectional area of profiles taken into account in the second joint penetration criterion.*

plete penetration until full joint penetration was obtained.

Figure 27 in the bottom row shows three typical cross-sections of the weld sample. In the top row, the corresponding brightness profiles of the image are shown. The decision on joint penetration was made by analyzing these profiles, as discussed earlier. Cross-section No. 85, a full penetration weld, was taken shortly after starting the welding with welding current about 385 A. Cross-section No. 106 was at the point where the incomplete joint penetration was detected with welding current about 350 A. Cross-section No. 124, a full penetration weld again, was the weld cross-section after welding current increased. The actual data for the above mentioned points with which the decision algorithm operated are summarized in Table 3, where brightness ratios, area, area ratio and the predetermined threshold values are given.

Because of noise in the radiographic images, the threshold values of area, area ratio and brightness ratio are important in detecting weld quality by this method. They are related to the detectability of a radiographic system as discussed previously. To have optimal control of weld quality, they must be selected carefully. It will be difficult to detect a small incomplete penetration using a very high threshold value. But, a very low threshold will make the penetration-control system very sensitive to radiographic noise. Several carefully controlled trial tests of joint penetration were needed to determine these threshold values.

As previously discussed, the system unsharpness value is another important factor, in addition to the noise level, in detecting small discontinuities. When incomplete penetration is very narrow and similar to or less than the system unsharpness value, the system unsharpness becomes vital. This is especially important for a weld joint with a narrow root opening. The linear compression of weld profiles may also decrease the resolution of the weld discontinuities, although it increases the processing speed.

The window of the image was selected at a distance (25 mm for the above case) behind the welding gun to avoid the "noisy" weld pool region. At this distance, the weld may be near to solidification. The effect of increasing welding current may not be able to recover the joint penetration, although it may decrease the incomplete penetration. A closer distance will help to give better control of joint penetration, but the effect of the noise from weld pool motions and gas bubbles must be considered. Another solution that overcame this disadvantage is discussed below.

**Table 3—Area, Area Ratio and Brightness Ratio**

| Profile | Area | | | | Area Ratio | Brightness Ratio |
|---|---|---|---|---|---|---|
| | (1)[a] | (2)[b] | (3)[c] | Ai | | |
| Threshold | 400 | 18 | | – | 0.1 | 0.1 |
| No. 85 | 543 | 24 | 23.2 | – | – | – |
| No. 106 | 590 | 24 | 25.7 | 41 | 0.065 | 0.476 |
| No. 124 | 700 | 32.8 | 26.7 | – | – | – |

(a) Column 1 shows area in threshold level pixel.
(b) Column 2 shows calculated area from data in Column 1 in $mm^2$.
(c) Column 3 shows actual measured area in weld cross-section in $mm^2$.

#### Preliminary Results on Control of Weld Penetration Based on Weld Pool Dimensions

The possibility of using information on dimensions of a depressed molten pool for radiographic control of a groove weld penetration was studied. The submerged arc welding process was used. The welding system and material were the same as in the experiments discussed previously.

The dimensions of the depressed pool surface of the groove weld were monitored by using the real-time radiographic system described in the previous sections. Using different welding currents and root openings, the resulting joint penetrations were changed. A greater welding current

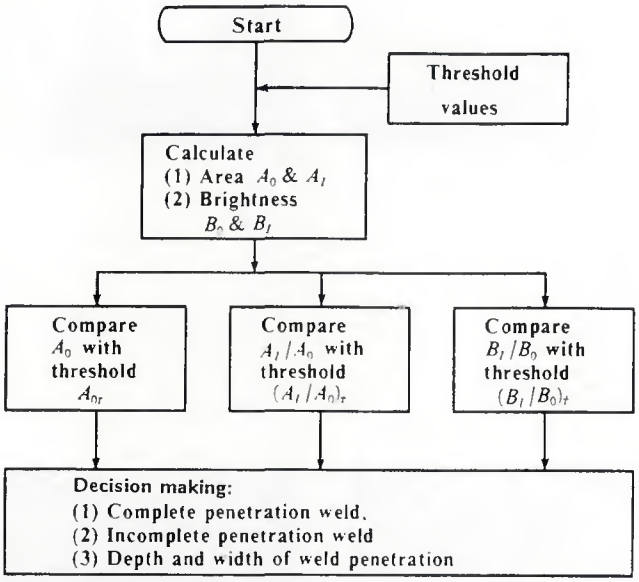


*Fig. 24 — Outline of the algorithm for deciding on the depth of joint penetration.*

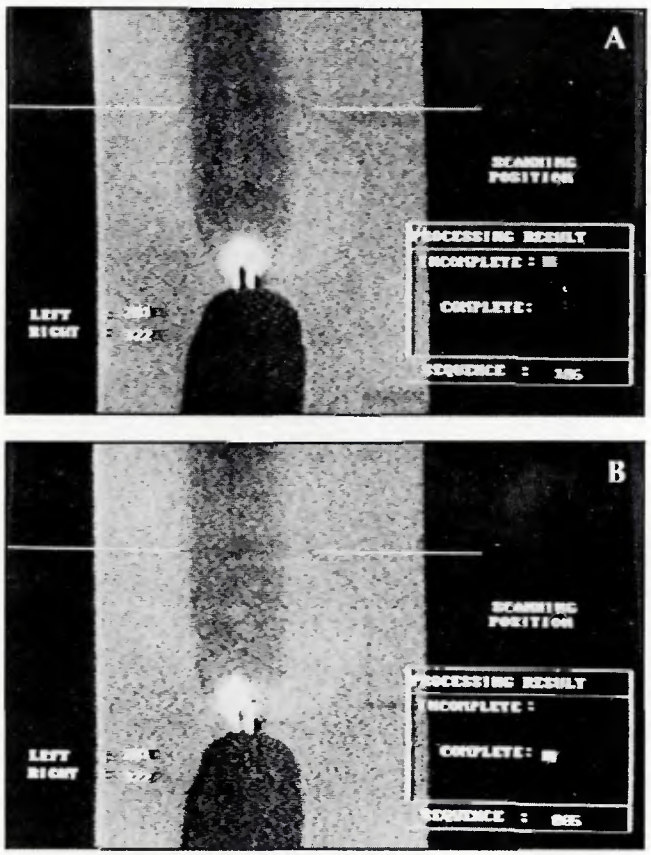


*Fig. 25 — Real-time radiographic image and computer decision overlay: A — incomplete (highlighted by box); B — complete.*

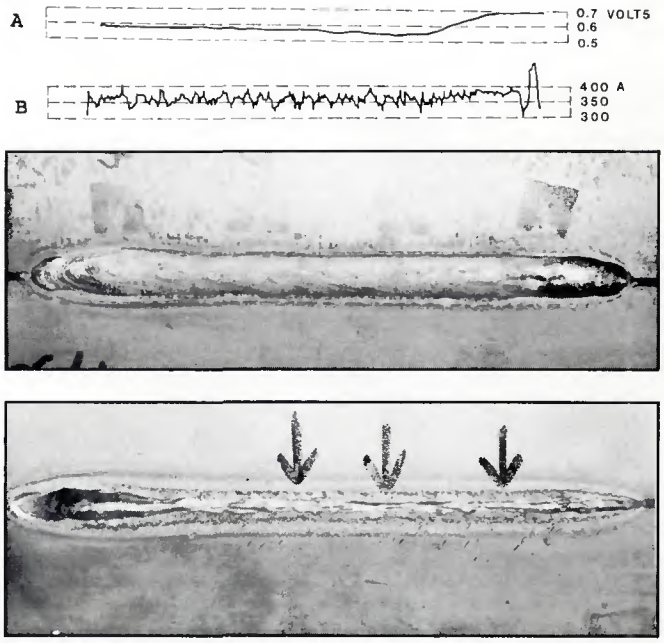


*Fig. 26 — A — Signal that controls welding current; B — actual measured welding current; C — photograph of weld sample (top and bottom view).*

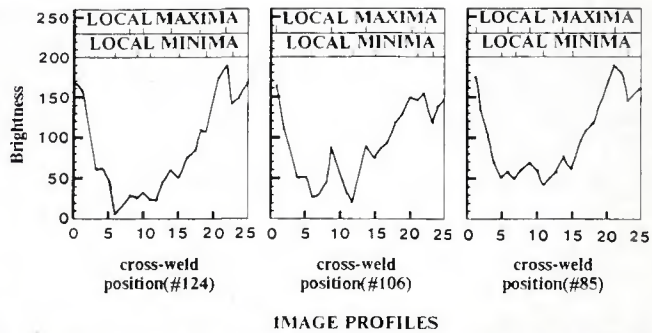


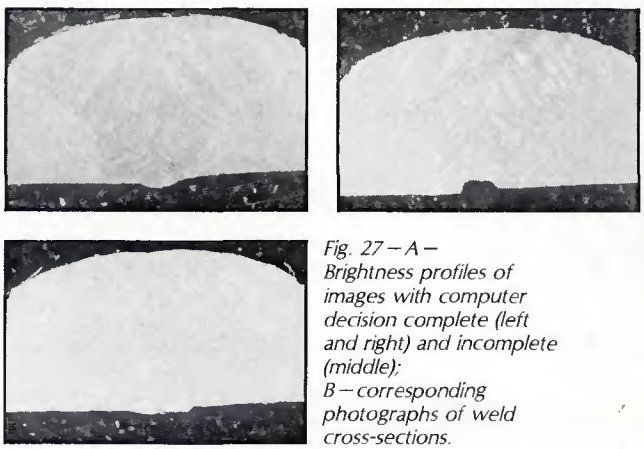

*Fig. 27 — A — Brightness profiles of images with computer decision complete (left and right) and incomplete (middle); B — corresponding photographs of weld cross-sections.*

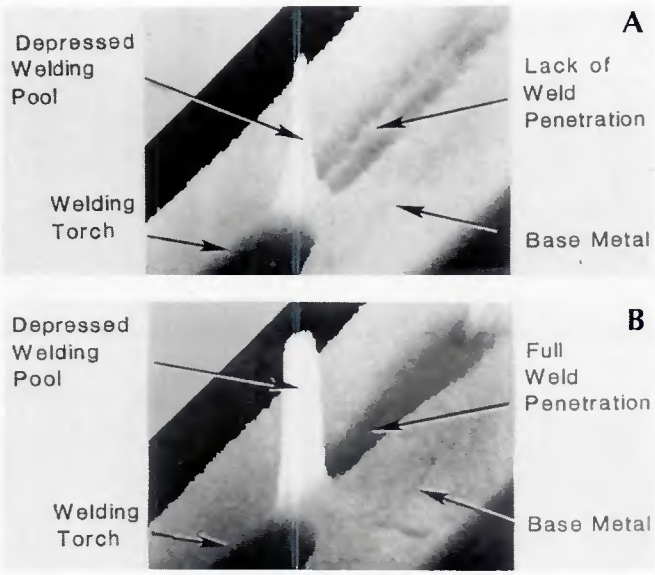


*Fig. 28 — Three-dimensional image of depressed pool of groove weld. A — Incomplete penetration groove weld; B — full penetration groove weld.*

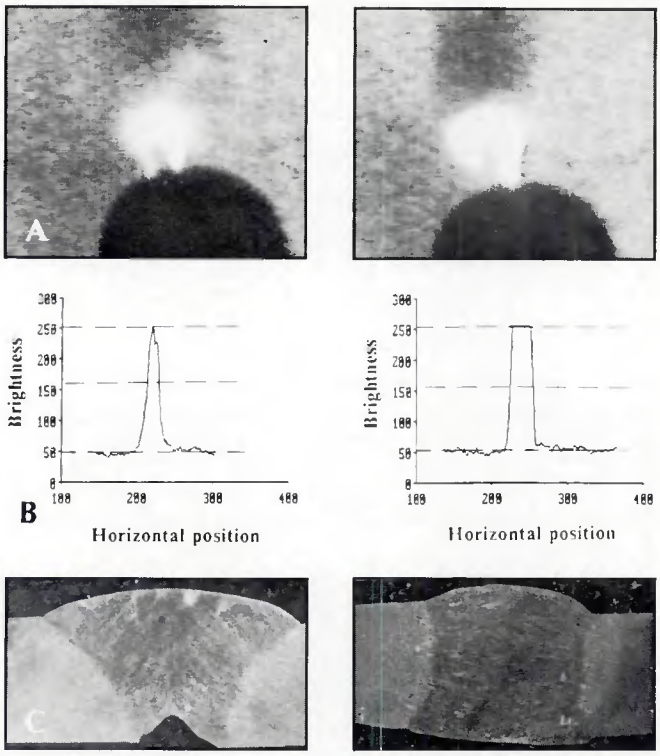


*Fig. 29 — A — Example of two real-time radiographic images of the pool depression for complete (right) and incomplete (left) weld; B — computer profile of brightness level through the middle of pool. (Units for the horizontal position in the radiographic profiles are in pixels. One pixel is 0.2 mm for the selected field of view); C — metallographs of the corresponding groove weld cross-sections showing complete (right) and incomplete (left) joint penetration.*

resulted in a larger pool diameter and full weld penetration.

Examples of two three-dimensional radiographic images are shown in Fig. 28. The light peak areas are images of depressed pools. It should be remembered that light areas correspond to reduced thickness of the material. The brightness of the weld pool means that the base metal melted and was pushed by plasma pressure away from the electrode, which may also be seen in these images. When the welding current is insufficient, melting of the base metal is less intense and the light area becomes narrower. In Fig. 28A, the incomplete penetration, shown as a white stripe, is visible. A groove weld with incomplete joint penetration shows the

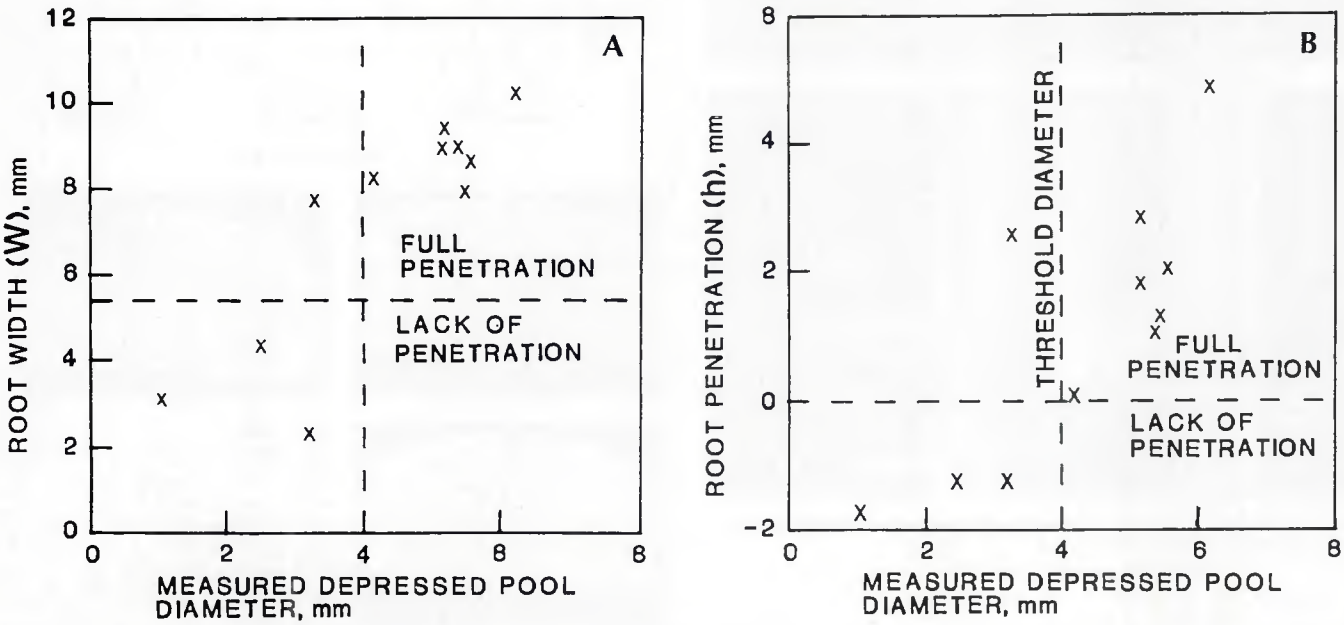


*Fig. 30 — A — Root width W and B — penetration depth h of groove weld obtained from cross-sections versus depressed pool diameter measured from real-time radiographic images.*

pool diameter as approximately the width of the root opening.

In Fig. 29, radiographic images (top) taken in the vicinity of the welding pool, and the metallographs of the corresponding weld cross-sections for full and partially penetrated welds are shown. The computer profiles (tracings) of the 3-D digitized images (Fig. 28) from the middle of the pool are shown. These may be used for quantitative measurement of the pool dimensions by the computer. Weld cross-sections (Fig. 29 C) clearly show that the left weld has incomplete penetration.

The results of the experiments are summarized in Fig. 30. In Fig. 30, the root width "W," incomplete joint penetration (−h), and the thickness of root penetration (+h) of the welds measured from metallographic cross-sections are plotted against depressed pool diameters measured from radiographs.

A preliminary study of the relationship between pool diameter and joint penetration has shown promising results. This method may be used to control weld reinforcement and penetration at the position immediately behind the welding electrode, eliminating delay in the control of the joint penetration. Conceptually, it is more effective to ensure the reinforcement of a weld and prevent incompleteness of joint penetration than to change welding parameters to their proper values after incomplete penetration occurs. A relationship between pool size and heat input may be established and will help to maintain the proper joint penetration. This concept can be used for control of joint penetration (Ref. 9). This type of measurement is also important for understanding arc-plasma pressure on the welding pool.

## Summary

The feasibility of real-time radiography has been demonstrated for on-line arc welding process study and control. An experimental system was developed that integrates the welding apparatus, x-ray, and image-intensifier units with a mechanical manipulator. A digital image processor and a variety of image storage and hard copy devices were used for image analysis and archiving.

A new concept of arc weld process control was developed for on-line control and maintenance of the appropriate weld quality. According to this concept, weld quality information extracted from real-time radiographic images and supplemented by sensor data on weld current and voltage is used for weld power supply control. The major differences from other welding control approaches is that closed-loop radiographic control, based on direct information on weld quality, is used. The concept was demonstrated for closed-loop process control of weld penetration is submerged arc welding.

Special software packages for on-line pattern recognition of incomplete joint penetration and control of the welding power supply were developed in the framework of this project. The capabilities of the method for the study of metal transfer and pool dynamics of arc welding were also demonstrated. In particular, it was shown that weld pool dimensions may be measured on-line.

*Acknowledgments*

This work was sponsored by the Edison Welding Institute. The assistance of Mr. Daniel Applegate and Mr. Kangra Cho in this research is greatly appreciated.

*References*

1. Watkins, A. D., Johnson, J. A., and Smart, H. B. 1986. Economic evaluation of concurrent welding and nondestructive testing. *Welding Journal* 65(6):17–21.

2. American Society for Nondestructive Testing. 1985. *Nondestructive Testing Handbook* Vol. 3, *Radiography and Radiation Testing*, Columbus, Ohio.

3. Becken, O. 1969. Material transfer from welding electrodes. International Institute of Welding Document 212-179-69.

4. Eichhorn, F., and Dilthey, V. 1971. High-speed x-ray photography for submerged arc welding. *Metal Construction and British Welding Journal* 3 (12):453–456.

5. Eichhorn, F., and Blasig, K. 1981. Process analysis in submerged arc welding with single and parallel strip electrodes. *Schweissen and Schneiden* 33 (1):9–13.

6. Bryant, L. E. 1971. Flash radiography of electron beam welding. *Materials Evaluation* 29(10):237–240.

7. Steinzel, A., and Thomer, G. 1961. X-ray flash cinematography up to 12,000 images/sec. *Journal of the Society of Motion Picture and Television Engineers* 70:18–20.

8. Panaitescu, I., and Rodean, E. 1977. Performance evaluation of radiographic system and techniques. *Research Techniques in NDT* Vol. 3, ed. R. S. Sharpe, Academic Press, New York.

9. Guu, A. C., and Rokhlin, S. I. 1989. Computerized radiographic weld penetration control with feedback on weld pool depression. *Materials Evaluation* 47(10), 1204–1210.